Applied Surface Science 626 (2023) 157205

Contents lists available at ScienceDirect

Applied Surface Science

journal homepage: www.elsevier.com/locate/apsusc

Full Length Article

Tailoring the deposition of $MoSe_2$ on TiO_2 nanorods arrays via radiofrequency magnetron sputtering for enhanced photoelectrochemical water splitting

Yahia H. Ahmad [a], Fadi Z. Kamand [b], Atef Zekri [c], Kyu-Jung Chae [d,e], Brahim Aïssa [c,*], Siham Y. Al-Qaradawi [a,*]

[a] Department of Chemistry and Earth Sciences, College of Arts and Sciences, Qatar University, Doha, P.O. Box 2713, Doha, Qatar
[b] Center for Advanced Materials, Qatar University, P.O. Box 2713, Doha, Qatar
[c] Qatar Environment & Energy Research Institute (QEERI), Hamad Bin Khalifa University (HBKU), Education City, P.O. Box 34110, Qatar Foundation, Doha, Qatar
[d] Department of Environmental Engineering, College of Ocean Science and Engineering, Korea Maritime and Ocean University, 727 Taejong-ro, Yeongdo-gu, Busan 49112, Republic of Korea
[e] Interdisciplinary Major of Ocean Renewable Energy Engineering, Korea Maritime and Ocean University, 727 Taejong-ro, Yeongdo-gu, Busan 49112, Republic of Korea

ARTICLE INFO

Keywords:
1D TiO_2 Nanorods
$MoSe_2$
Radiofrequency magnetron sputtering
Heterojunction
Photoelectrochemical water splitting

ABSTRACT

$MoSe_2$/1 D TiO2 nanorods (NRs) heterojunction assembly was systematically fabricated, and its photoelectrocatalytic properties were investigated. The fabrication process involves the growth of 1D TiO_2 NRs arrays on FTO substrates using hydrothermal synthesis followed by the deposition of $MoSe_2$ nanosheets on the TiO_2 NRs using radiofrequency magnetron sputtering (RF magnetron sputtering). The photoelectrochemical properties of the heterojunction were explored and optimized as a function of the thickness of the $MoSe_2$ layer, which was controlled by the sputtering time. The $MoSe_2$ grows perpendicularly on TiO_2 NRs in a 2D layered structure, maximizing the exposed active edges, an essential aspect that permits maximum exploitation of deposited $MoSe_2$.

Compared to pure TiO_2 NRs, the heterojunction nanostructured assembly displayed excellent spectral and photoelectrochemical properties, including more surface oxygen vacancies, enhanced visible-light absorption, higher photocurrent response, and decreased charge transfer resistance. In particular, the sample synthesized by sputtering of $MoSe_2$ for 90 s, i.e., $MoSe_2$@TiO_2-90 s, depicted the highest current density (1.86 mA cm^{-2} at 0.5 V vs. Ag/AgCl) compared to other samples.

The excellent photoelectrochemical activity of the heterojunction stemmed from the synergy between tailored loading of $MoSe_2$ nanosheets and the 1D structure of TiO_2 NRs, which afford a high surface/volume ratio, effective charge separation, fast electron transfer, and easy accessibility to the $MoSe_2$ active edges. These factors boost the catalytic activity.

1. Introduction

In the last decades, enormous efforts have been exerted to develop clean, renewable energy sources that can replace extensively polluting exhaustible fossil fuels. On a broad scale, hydrogen as a clean fuel represents a promising candidate that can supply clean energy without deteriorating the environment. In this regard, different approaches were employed for hydrogen production. Among them, the most applied approaches on the industrial scale are the steam reforming of methane, partial oxidation of hydrocarbons, and coal gasification [1]. However, despite their cost-effectiveness, these approaches endow the generation of large amounts of CO_2 [2]. Alternatively, other approaches, such as water electrolysis, can be considered an alternative environmentally benign route devoted to producing clean high-purity hydrogen [3,4].

Photoelectrolysis of water is a promising technology aiming at obtaining hydrogen and oxygen through solar energy harvesting by a semiconductor, which acts as a photocatalyst [5]. Since Honda and Fujishima [6] demonstrated the primitive photocatalytic water splitting by TiO_2, extensive efforts have been devoted to developing photoelectrodes capable of delivering high solar-to-hydrogen efficiency. As a result, TiO_2 is regarded as one of the most investigated materials in photoelectrolysis, assigned to its chemical stability, increased

* Corresponding authors.
E-mail addresses: baissa@hbku.edu.qa (B. Aïssa), siham@qu.edu.qa (S.Y. Al-Qaradawi).

https://doi.org/10.1016/j.apsusc.2023.157205
Received 11 January 2023; Received in revised form 19 March 2023; Accepted 3 April 2023
Available online 7 April 2023

abundance, enhanced photocatalytic activity, biocompatibility, and reasonable cost [7,8]. However, its relatively wide band gap, which limits its light absorption to the ultraviolet region, and the short lifetime of photo-induced charge carriers are considered the main drawbacks limiting its efficiency in different photocatalytic applications [9]. In this regard, several approaches were hired to decrease the bandgap and inhibit the fast recombination of photo-induced electrons and holes, such as doping with metals and non-metals [10], formation of nanostructures [11], coupling to a co-catalyst [12,13], and coupling with another semiconductor to form heterojunction, which is considered as one of the most effective strategies to enhance the photocatalytic activity [14,15].

Recently, 2D transition metals chalcogenides (TMCs) have emerged as promising candidates for versatile applications such as optoelectronics, sensing, energy storage, and catalysis [16–22]. In particular, their application in photocatalysis has remarkably emerged owing to their narrow band gap and 2D graphene-like structure, which can act as an electron bridge facilitating the electron transfer of the photo-induced charge carriers [23]. 2D TMCs have a layered structure with a chemical composition of MX_2 (where M is the transition metal, and X = S, Se, or Te) [24,25]. Among them, $MoSe_2$ has recently received increasing interest inspired by its low band gap of 1.7–1.9 eV, fast photo-response, and high conductivity attributed to the metallic characteristics of Se atoms [26,27].

$MoSe_2$ consists of a Mo layer sandwiched between two layers of Se. It can exist in two phases: the semiconducting 2H phase, which has a trigonal prismatic structure, and the metallic 1 T phase, which has distorted octahedral geometry. The metallic 1 T form is metastable and can be easily converted to the more stable 2H structure [28]. Despite its outstanding properties, such as the narrow band gap and high resistance towards photocorrosion [29,30], $MoSe_2$ is encountered by inferior photocatalytic performance attributed to its slow rate of charge transfer and fast recombination of photo-generated charges [31]. Accordingly, coupling $MoSe_2$ to other semiconductors, such as TiO_2, can afford enhanced charge transfer, charge separation, and photocatalytic performance [32].

The $MoSe_2/TiO_2$ heterostructure is an affordable promising candidate for photoelectrochemical water splitting. Different studies reported the synthesis of $MoSe_2/TiO_2$ for various photocatalytic applications [33]. For instance, R. Zazpe et al. studied the deposition of $MoSe_2$ nanosheets on TiO_2 nanotubes using atomic layer deposition [34]. They found that the $MoSe_2$ grows at the inner and outer surfaces of the TiO_2 nanotubes in a perpendicular orientation which maximizes the exposed $MoSe_2$ active edges and enhances its activity towards photocatalytic degradation of methylene blue and electrochemical hydrogen evolution in an acidic medium [34]. Similarly, $MoSe_2$ was deposited on TiO_2 nanotubes via electrochemical deposition from an aqueous solution containing Na_2MoO_4, SeO_2, and H_3PO_4 [35]. The multifunctional anode revealed enhanced activity towards photoelectrochemical degradation of cefotaxime sodium at low applied voltages, which was assigned to the synergism between the surface oxygen vacancies and the charge separation originated by direct Z-scheme of $TiO_2/MoSe_2$ heterojunction [35].

Intriguingly, several approaches were dedicated to the synthesis of $MoSe_2$ layers, such as sonochemical synthesis, chemical vapor deposition [36], solvothermal [37], magnetron sputtering [38], and exfoliation of bulk $MoSe_2$ [39]. However, most of these methods are sophisticated or afford a bulk form of stacked multilayered material with minimum exposed active sites and inferior catalytic activity. Among them, magnetron sputtering offers several merits, such as precise control of the structure/thickness of the deposited layer, modulated electrical/optical properties, high surface area, and strong adhesion [40]. In addition, they produce nanostructured $MoSe_2$ layers with a high density of exposed active edges. Although some studies reported the synthesis of $MoSe_2$ by radiofrequency magnetron sputtering (RF magnetron sputtering), however, deposition of $MoSe_2$ by RF magnetron sputtering on TiO_2 nanostructures was rarely reported [41], and application of such heterostructures in photoelectrochemical water splitting was not previously reported.

Triggered by these discussions, herein, we introduce the fabrication of $MoSe_2$/1D TiO_2 NRs using RF magnetron sputtering of $MoSe_2$ target on TiO_2 NRs arrays and explore their activity towards photoelectrochemical water splitting. The novelty of this study emerges from employing RF magnetron sputtering approach to tune the deposition of $MoSe_2$ nanosheets on 1D TiO_2 NRs arrays. The photoelectrochemical activity of the heterojunction was optimized through the control of the sputtering time. RF magnetron sputtering enables not only precise control on the thickness of $MoSe_2$ layer on the TiO_2 NRs but also allows the control of the 2D surface structure, which is pivotal for photocatalytic activity. The superior photoelectrochemical activity arises from the synergy between the 1D TiO_2 nanostructure and the tailored structure of $MoSe_2$ layers, which afford extensive active centers and fast electron transfer boosting the catalytic activity.

2. Experimental

2.1. Materials synthesis

2.1.1. Synthesis of vertically oriented 1D TiO_2 NRs

Firstly, FTO substrates (20 mm × 15 mm, 6.70 ± 0.27 Ω/sq, Ossila Ltd., Sheffield, UK) were cleaned by ultrasonication for 20 min in acetone, ethanol, and deionized water, respectively, and finally dried in air.

In a glass beaker, 25 mL of deionized water was mixed with 25 mL of concentrated HCl with stirring. To the formed solution, 300 μL of titanium (IV) butoxide was added, and the solution was stirred for further 5 min. After mixing, the solution was transferred into a Teflon-lined stainless steel autoclave, and FTO substrates were immersed into the solution in such a way that the conducting sides faced the bottom of the autoclave. The autoclave was sealed and heated in an oven at 160 °C for 10 h. Afterward, the autoclave was allowed to cool to room temperature, and the substrates were washed with DI water and ethanol and calcined in air at 400 °C for 3 h using a ramping rate of 1 °C min^{-1}.

2.1.2. Synthesis of $MoSe_2$@TiO_2 NRs

The $MoSe_2$ layers were deposited onto TiO_2 NRs via RF magnetron sputtering (Torr International Services LLC, USA) using a high purity target (99.95 %, 50.8 mm diameter, 4 mm thickness, Able Target Limited, Nanjing, China) at a temperature of 200 °C, under high purity argon as bombarding gas. Prior to sputtering, the chamber was evacuated to a pressure of $3x10^{-5}$ Torr using a turbomolecular pump. During the deposition, a flow of Ar gas was maintained at a rate of 10 sccm, the applied power was adjusted at 200 W, and the temperature was maintained at 200 °C. The thickness of deposited $MoSe_2$ was controlled by varying the sputtering time between 15 s and 120 s, and the samples produced by applying a sputtering time of 15 s, 30 s, 60 s, 90 s, and 120 s were denoted as $MoSe_2$@TiO_2-15 s, $MoSe_2$@TiO_2-30 s, $MoSe_2$@TiO_2-60 s, $MoSe_2$@TiO_2-90 s, and $MoSe_2$@TiO_2-120 s, respectively. For comparison, $MoSe_2$ was sputtered on FTO glass for 90 s, and its spectral and photoelectrochemical characteristics were investigated.

2.2. Characterization

The morphology and microstructure of as-prepared samples were characterized by a field emission scanning electron microscope (FESEM) equipped with an energy-dispersive X-ray (EDX) unit. Raman spectra were examined using a DXR Raman microscope (ThermoScientific) using a laser excitation beam with a wavelength of 532 nm. The crystallinity of samples was investigated by X-ray diffraction (XRD) using an X'Pert Phillips diffractometer equipped with Cu-kα radiation (λ = 1.54059 Å) (Phillips-PANalytical, Netherlands). The electronic structures and oxidation states were investigated by X-ray photoelectron

spectroscopy (XPS) with Axis Ultra DLD XPS (Kratos, Manchester, UK) equipped with a monochromatic Al-Kα radiation source (1486.6 eV). All binding energies were corrected with reference standard C 1 s peak, i.e., 284.6 eV. UV–Visible spectra were recorded using a UV/Vis/NIR spectrophotometer (Perkin Elmer, Lamda 1050, USA).

2.3. Photoelectrochemical measurements

Photoelectrochemical measurements were conducted using Gamry 3000 workstation (Gamry Co., USA). Measurements were conducted in a standard three-electrode cell with a quartz window. The as-prepared electrode, platinum wire, and Ag/AgCl electrode were used as photoanode, counter electrode, and reference electrode, respectively. The photocurrent response (current vs. time, I-t) plots were measured in 1.0 M KOH solution under simulated solar light irradiation (light/dark cycles of 30 s). Electrochemical impedance spectroscopy (EIS) measurements were recorded in the frequency range of 0.1 and 10^5 Hz at a potential of 0.5 V vs. Ag/AgCl using an excitation AC signal with an amplitude of 5 mV. The type of semiconductor and the flat band potentials were investigated using Mott-Schottky (MS) analysis. Measurements were performed in 1.0 M KOH solution at a scan frequency of 1000 Hz. Potential measurements were referenced to a reference hydrogen electrode (RHE) [42] according to the relation:

$$E_{RHE} = E_{Ag/AgCl} + 0.197 + 0.059\ pH.$$

3. Results and discussion

TiO_2 nanostructures were devoted to versatile applications such as sensors, optoelectronic devices, and solar cells [43]. Among them, one-dimensional nanostructures aroused great interest attributed to their directional charge transmission properties originating from the quantum confinement effect. In particular, nanorods exhibited several merits, such as dense structure, high aspect ratio, and large specific surface area [44]. This results in effective photogenerated charge separation and light absorption, which are essential for potential applications of TiO_2-based materials, especially photocatalytic applications.

TiO_2 NRs arrays were synthesized on FTO substrates using the hydrothermal method. During the process, The butoxide precursor is firstly hydrolyzed to form hydroxocomplexes in the solution. The hydroxocomplexes are known as the building units for the formation of 1D TiO_2 nanostructures. They are protonated and undergo dehydration (condensation) reactions to produce polymeric 1D TiO_2 nanostructures through the formation of Ti-O-Ti bridged bonds [45]. It should be noted that in a highly acidic environment, the rutile phase is pertinent, while in weakly acidic media, anatase is the predominant phase [46,47].

2D $MoSe_2$ can deliver unparalleled merits compared to bulk $MoSe_2$, which has limited reactivity owing to inert basal planes. Among the merits of 2D material, the high surface area-to-volume ratio and the high density of defects originated at the edges of the nanosheets. These defects are considered active sites for different catalytic reactions, attributed to the high abundance of active centers with low coordination numbers, represented by defects, kinks, and edges responsible for the high catalytic activity. It should be noted that controlling the thickness (number of layers) of $MoSe_2$ via RF magnetron sputtering not only produces 2D layers (Fig. S1) of tunable band gap, but also it can switch the band structure from indirect (bulk material) to direct (monolayer structure), which renders $MoSe_2$ extraordinary candidate for several electrical and optical applications [26].

The structure and morphology of TiO_2 NRs and MoSe@TiO_2 NRs were investigated by SEM. Fig. 1a-c depict the FESEM images of TiO_2 NRs grown on FTO substrate at 150 °C for 10 h. The top view of pure TiO_2 NRs (Fig. 1a and b) exhibits vertically oriented densely packed nanorods with tetragonal shape and square top surfaces. The top surfaces contained several step edges, while the side view revealed smooth side surfaces (Fig. 1c).

The nanorods show an average length of 3.4 ± 0.5 μm, estimated from the side view of the cross-sectional image; however, they manifested wide diversity in the diameters of NRs ranging between 40 and 300 nm. Furthermore, the deposition of $MoSe_2$ did not affect the morphology of the TiO_2 NRs, and no difference was observed in the SEM images of pure TiO_2 NRs compared to the nanocomposite. This reveals the uniform homogenous distribution of $MoSe_2$ on the surface of TiO_2 NRs arrays, which is one of the main advantages of magnetron sputtering compared to other techniques (Fig. 1d-f).

The structure and morphology were further investigated by TEM (Figs. 2, 3, S2 and S3). The selected area electron diffraction (SAED) pattern of TiO_2 NRs (stripped from the substrate) shows well-defined sharp patterns indexed to the rutile TiO_2 (Fig. 2a inset), which is consistent with the results of XRD. The high-resolution TEM (HR-TEM) image is given in Fig. 2a. It shows well-ordered clear lattice fringes confirming the crystalline nature of TiO_2 NRs. The lattice spacing between two adjacent fringes is about 0.32 nm lattice fringes, which

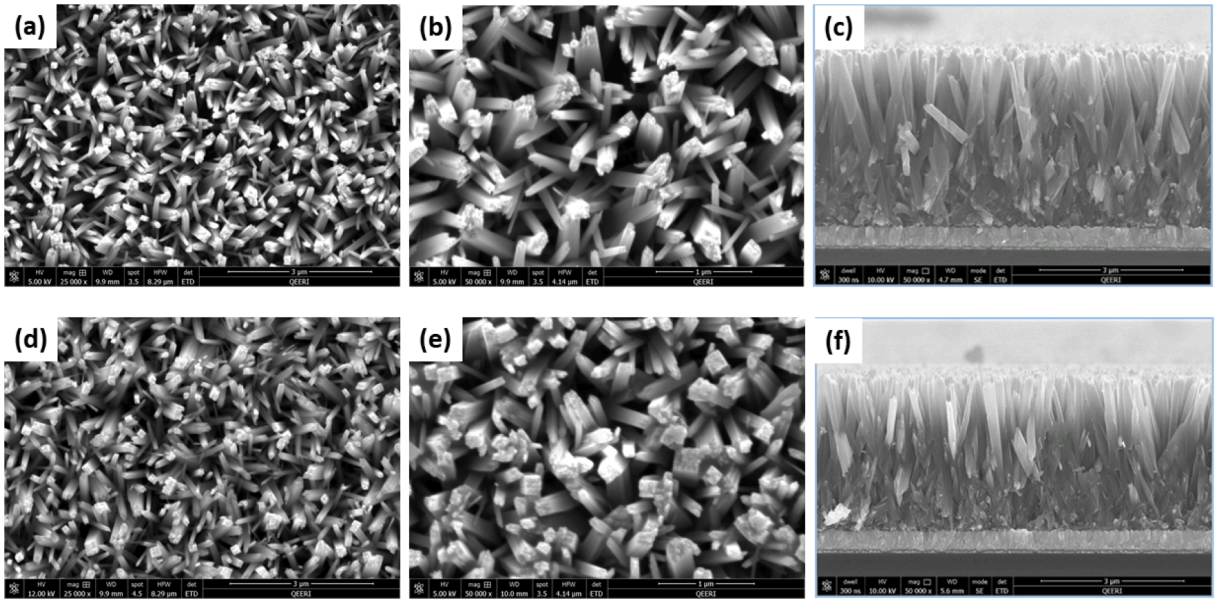

Fig. 1. SEM images of TiO_2 NRs; top view (a and b) and side view (c) and $MoSe_2$@TiO_2 NRs top view (d and e) and side view (f).

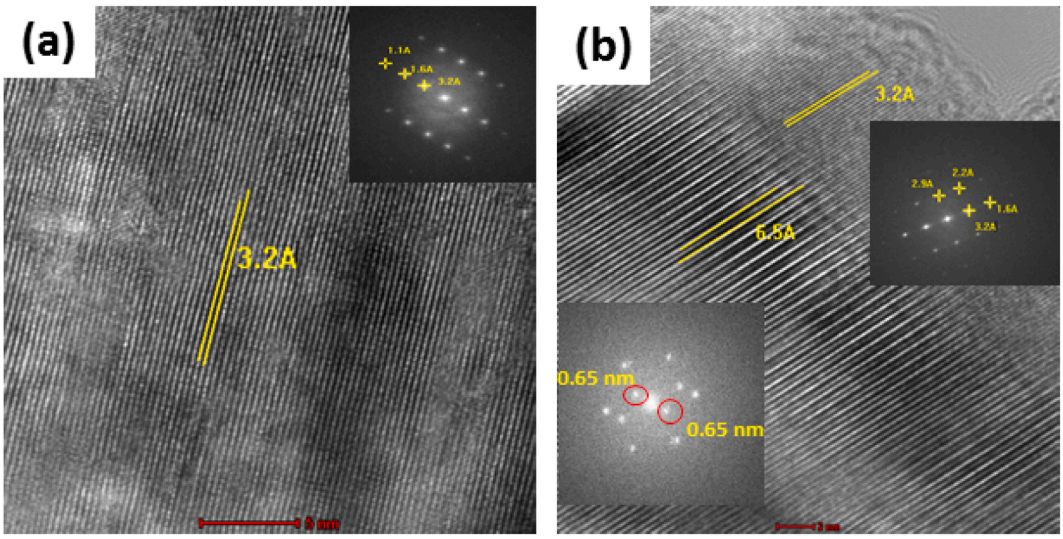

Fig. 2. HRTEM and SAED patterns of (a) TiO_2 NRs and (b) $MoSe_2$@TiO_2 NRs.

corresponds to the distance between (1 1 0) lattice planes of rutile [48]. The HRTEM image of $MoSe_2$@TiO_2 (Fig. 2b) clearly identifies lattice fringes with a spacing of 0.32 nm assigned to rutile and another set with a spacing of 0.65 nm, which can be indexed the (0 0 2) plane of hexagonal $MoSe_2$ [49]. The distribution of elements within the heterostructure was evaluated via HAADF-STEM-EDS elemental mapping (Fig. 3). Images depicted a uniform distribution of $MoSe_2$ over the TiO_2 nanorods.

The surface chemical composition was examined by XPS. The survey spectrum of TiO_2 NRs and $MoSe_2$@TiO_2 NRs illustrates the presence of C, Ti, and O in pristine TiO_2 NRs and the presence of Mo, C, Ti, O, and Se in the case of the heterostructure, confirming their purity. Deconvolution of the Ti 2p high-resolution spectrum of $MoSe_2$/TiO_2 NRs showed four peaks (Fig. 4a). Two peaks at 458.6 eV and 464.5, corresponding to Ti^{4+} of Ti − O − Ti, and the other two peaks of lower intensities at 459.8 and 465.8 eV, corresponding to Ti^{4+} of Ti − O − Mo [50]. The Gaussian peak fitting of O 1 s in the heterostructure (Fig. 4b) revealed four different components at 529.9, 530.7, 531.6, and 532.9 eV, assigned to the lattice oxygen (O^{2-}) from Ti − O − Ti bond, lattice oxygen from Ti − O − Mo bond, oxygen defects (vacancies), and adsorbed oxygenated species, respectively [51,52].

Fig. 4c and S4a shows the deconvolution of the high-resolution Mo 3d spectrum in the heterojunction and pure $MoSe_2$, respectively. It revealed two main peaks at 228.8 and 231.9 eV corresponding to Mo^{4+}, in addition to two small peaks at 230.1 and 233.7 eV, that can be assigned to Mo^{6+} [36]. On the other hand, the Se XPS spectrum (Fig. 4d and S4b) depicts two peaks at 54.1 and 55.0 eV assigned to Se $3d_{5/2}$ and Se $3d_{3/2}$ of Se^{2-}, respectively [53]. The high-resolution spectrum of Ti 2p in the pristine TiO_2 NRs (Fig. S5) shows two peaks at 459.4 and 465.2 eV, which can be indexed to Ti $2p_{3/2}$ and Ti $2p_{1/2}$ of Ti^{4+}, respectively [54]. The binding energies of Ti 2p core levels in the heterostructure are shifted to lower values compared to pure TiO_2, which can be assigned to the enhanced electron interaction between TiO_2 and $MoSe_2$ (Fig. S6) [33].

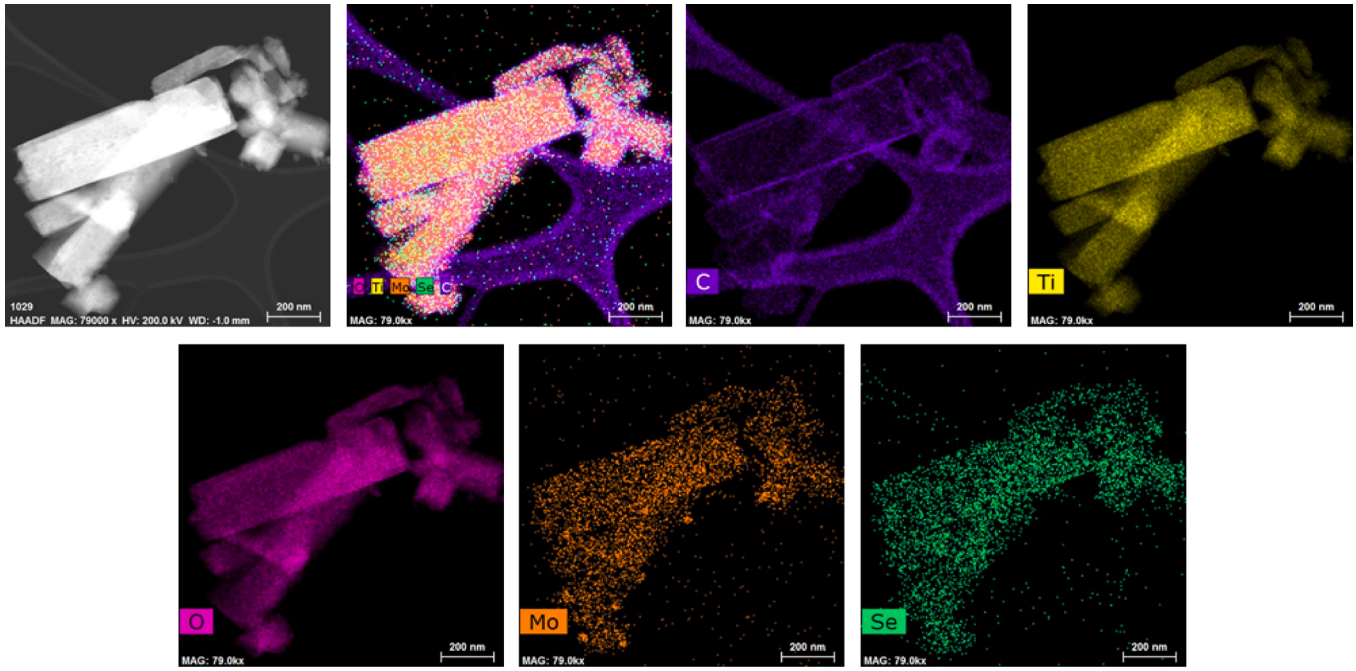

Fig. 3. HAADF-EDS elemental mapping in $MoSe_2$@TiO_2 NRs.

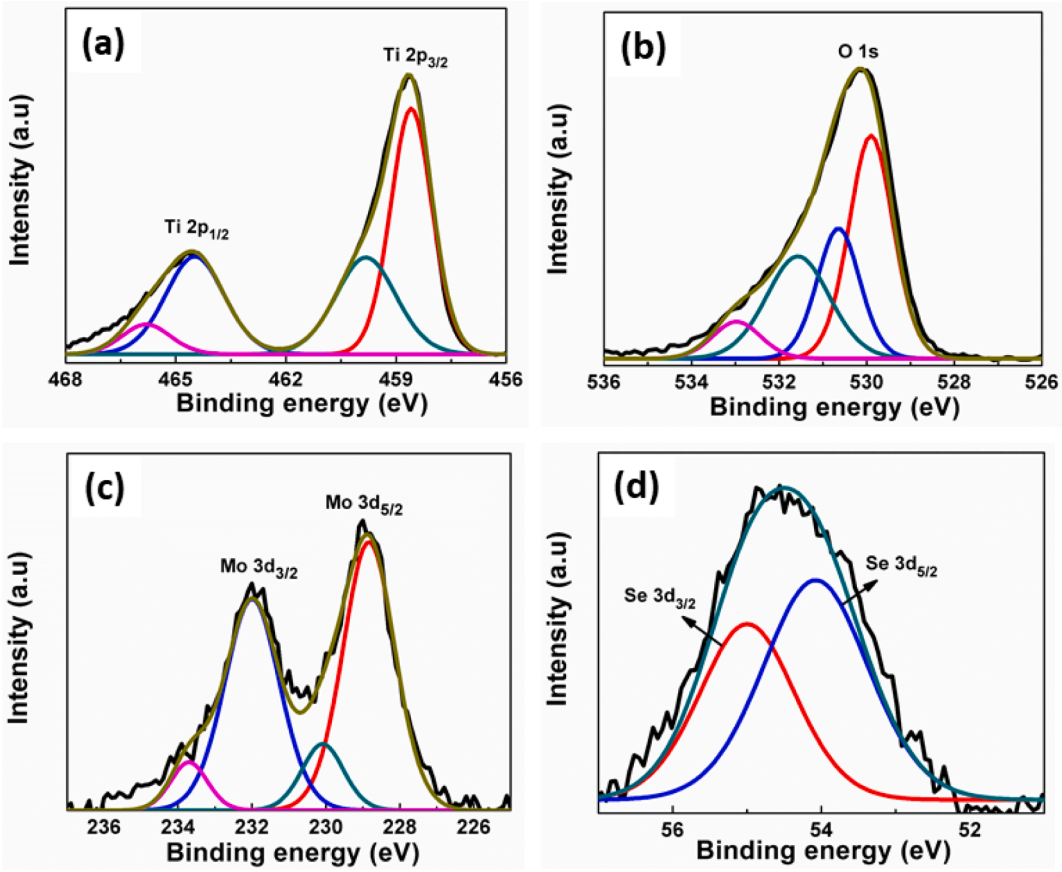

Fig. 4. High resolution XPS spectra of (a) Ti 2p and (b) O 1 s, (c) Mo 3d, and (d) Se 3d in $MoSe_2/TiO_2$ NRs.

The crystalline structure of TiO_2 NRs and $MoSe_2$@TiO_2 NRs was studied by XRD (Fig. 5). All samples revealed diffraction peaks at about 26.5, 33.7, 37.7, 51.5, 54.5, 61.5, 65.5, and 78.2°, which are assigned to (1 1 0), (1 0 1), (2 0 0), (2 1 1), (2 2 0), (3 1 0), (3 0 1), and (3 2 1) planes of tetragonal SnO_2 structure, respectively (JCPDS card no. 041–1445) and originated from the FTO substrate [55]. Furthermore, all catalysts exhibited a single crystalline rutile structure with an intense diffraction peak at 2θ of about 36.1° assigned to the (1 0 1) plane of the tetragonal structure of the rutile phase (JCPDS card no. 21–1276) [56,57]. The minor diffractions observed at 2θ of 62.8, 69.8, and 69.9° can be indexed to (0 0 2), (3 0 1), and (1 1 2) planes of rutile, respectively. No observable diffraction peaks were detected for $MoSe_2$ in the heterojunction structures (Fig. 5) or pure $MoSe_2$ (Fig. S7). This may be attributed to the low crystallinity of $MoSe_2$ and/or the ultrathin few-layer structure, which is consistent with previous studies [31,58].

Fig. 6 represents the Raman spectrum of TiO_2 NRs and the different heterojunction photocatalysts. All photocatalysts revealed three Raman peaks at about 233, 447, and 613 cm^{-1}, which can be assigned to two phonon scattering, out-of-plane vibration (A1g), and in-plane vibration (Eg) of rutile phase [59,60].

No Raman peaks were detected for $MoSe_2$ owing to their few-layer structure, which is in agreement with previous reports [31].

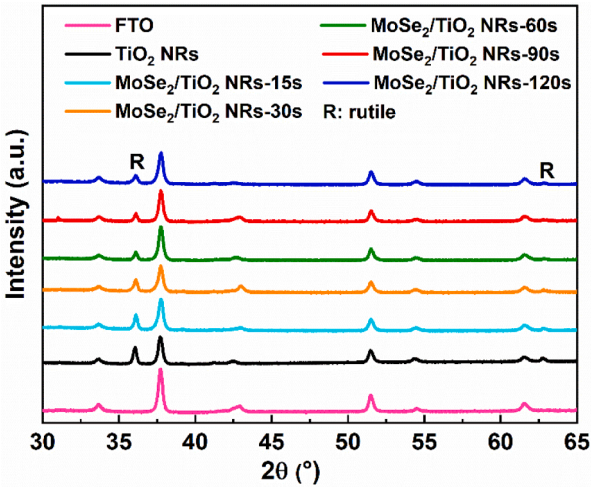

Fig. 5. XRD spectra of investigated photocatalysts.

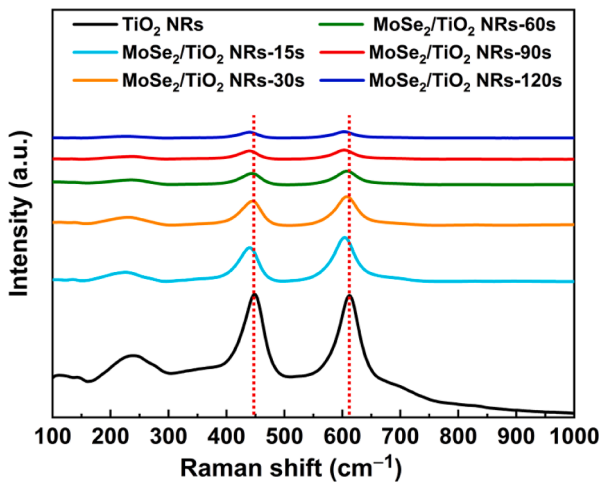

Fig. 6. Raman spectra of the investigated photocatalysts.

Interestingly, the intensity of rutile peaks decreased after the deposition of $MoSe_2$, in addition, the Raman peaks are shifted to lower wavenumbers confirming the electronic interaction between TiO_2 and $MoSe_2$.

Light absorption is a crucial factor that remarkably affects the photocatalytic activity. The UV/Vis diffuse reflectance spectra of TiO_2 NRs and the other heterostructures are depicted in Fig. 7. Results revealed that the optical absorption of the material increased in the visible as the deposition time of $MoSe_2$ increased. In other words, the heterostructured photocatalysts have higher optical absorption in the visible region than pure TiO_2 NRs. This absorption increases with the increase in the thickness of $MoSe_2$. The optical band gaps of photocatalysts were determined from Tauc plots (Fig. S3). Tauc equation can be given as:

$$\alpha h\nu = C(h\nu - E_g)^{n/2}$$

where α is the absorption coefficient, h is Planck's constant, ν is the frequency, Eg is the band gap energy, C is a constant, and the coefficient n is n = 1 for direct transition and n = 4 for indirect transition in a semiconductor. TiO_2 has indirect band gap, hence, the value of n is 4.

This rise was observed at high wavelengths in all samples, including pure TiO_2 NRs and all $MoSe_2/TiO_2$ electrodes. However, this rise was not observed in the FTO substrate (Fig. S8). This tail-up was observed in previous studies for rutile nanorods in previous studies [61,62]. It was attributed to the lattice defects such as oxygen vacancies [63]. The band gap energies were calculated by plotting $(\alpha h\nu)^{1/2}$ vs. the photon energy, $h\nu$, where the intercepts of the plots define the band energies (Fig. S9). The calculated values of band gap energies were found to be 3.05, 3.01, 2.95, 2.87, 2.72, and 2.60 eV, in the case of TiO_2 NRs, $MoSe_2/TiO_2$-15 s, $MoSe_2/TiO_2$-30 s, $MoSe_2/TiO_2$-60 s, $MoSe_2/TiO_2$-90 s, and $MoSe_2/TiO_2$-120 s, respectively. This confirms the enhancement in the light absorption by successive deposition of $MoSe_2$ layers on TiO_2 NRs. Similarly, the band gap energy of pure MoSe2 was calculated from Tauc plot and was found to be 1.89 eV (Fig. S10).

In order to investigate the impact of $MoSe_2$ and its thickness on the photocatalytic activity, the electrochemical performance of TiO_2 NRs and different heterojunction electrodes was investigated towards photoelectrochemical water splitting. Linear sweep voltammetry (LSV) is a common tool for evaluating the charge transfer characteristics at the semiconductor/electrolyte interface. Fig. 8a represents the LSV curves of different electrodes, recorded under illumination with (AM 1.5G, 100 mW cm^{-2}) simulated sunlight in 1.0 M KOH solution. To verify the negligible leakage current, measurements were performed in the dark at the same potential range (Fig. S11) [64]. The recorded voltammograms an insignificant increase in the current from 0.5 V up to 2.0 V vs. RHE, where the current start to increase owing to the start of electrochemical oxygen evolution.

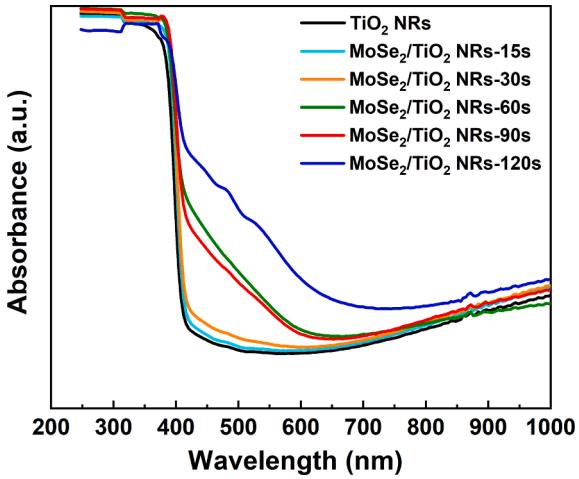

Fig. 7. Uv–vis reflectance spectra of the studied photocatalysts.

Under illumination, all photocatalysts revealed a pronounced photocurrent starting at 0.3 V vs. RHE and continued to increase, reaching a saturation value at about 0.9 V vs. RHE. Pure TiO_2 NRs delivered a saturation photocurrent density of 0.48 mA cm^{-2}. It is noticeable that the saturation photocurrent increases with increasing the thickness of sputtered $MoSe_2$ layers on TiO_2 NRs, reaching a maximum at $MoSe_2/TiO_2$ NRs-90 s, which afforded a saturation photocurrent density of 1.71 mA cm^{-2}, which is almost 3.6 folds higher than pure TiO_2 NRs. This remarkable enhancement in the photocurrent density of the heterojunction compared to pure TiO_2 NRs can be attributed to the enhanced charge separation owing to the formation of Z-scheme heterojunction and the promoted light absorption. These results confirm that the PEC performance of $MoSe_2/TiO_2$ heterostructure can be optimized by controlling the amount (thickness) of $MoSe_2$ layer on the surface of TiO_2 NRs. The saturation photocurrent decreases at higher sputtering times, which can be assigned to the hindering of the light absorption by excessive $MoSe_2$ layers and reduce the photocurrent density [65].

For further investigating the impact of $MoSe_2$ on the photoactivity of TiO_2 NRs, the photocurrent response over time was examined by amperometric J-t curves, collected with light on–off cycles at a potential of 0.5 V vs. Ag/AgCl in 1.0 M KOH solution (Fig. 8b). At the dark state, all electrodes exhibited very small current densities. When the light was switched on, the current density rapidly increased owing to the creation of hole/electron pairs, enhancing the current density. The heterostructures delivered higher photocurrent density compared to pure TiO_2 NRs. The measured photocurrent densities at 0.5 V vs. Ag/AgCl are for 0.47, 0.66, 0.88, 1.42, 1.86, and 1.66 mA cm^{-2}, for TiO_2 NRs, $MoSe_2/TiO_2$ NRs-15 s, $MoSe_2/TiO_2$ NRs-30 s, $MoSe_2/TiO_2$ NRs-60 s, $MoSe_2/TiO_2$ NRs-90 s, and $MoSe_2/TiO_2$ NRs-120 s, respectively. No significant decay occurs over the measurement period, implying the enhanced stability of electrodes towards photocorrosion.

EIS was hired to evaluate the interfacial charge transfer kinetics of the investigated photocatalysts. Fig. 8c represents the Nyquist impedance plots of different electrodes in 1 M KOH solution at 0.5 V vs. Ag/AgCl. Semicircles of variable radii were observed for the studied materials, which confirms that the kinetics is dominated by the charge transfer process at the electrode/electrolyte interface [66]. The radius of these semicircles follows the order: TiO_2 NRs > $MoSe_2/TiO_2$ NRs-15 s > $MoSe_2/TiO_2$ NRs-30 s > $MoSe_2/TiO_2$ NRs-60 s > $MoSe_2/TiO_2$ NRs-120 s > $MoSe_2/TiO_2$ NRs-90 s. It is widely accepted that the small radius of the Nyquist plot represents lower charge transfer resistance and faster reaction kinetics [67]. Therefore, increasing the thickness of $MoSe_2$, decreases the charge transfer resistance and enhances the kinetics, which reaches a maximum for $MoSe_2/TiO_2$ NRs-90 s. Higher thicknesses of $MoSe_2$ increase the charge transfer resistance and the recombination rate of photo-induced charges, decreasing the photocatalytic activity.

The measured impedance data were fitted to different equivalent circuit models, and the model which provided the best fitting is represented in Fig. S12 [68]. The calculated charge transfer resistances from data fitting (Fig. S13) are 7.89 kΩ cm^{-2}, 4.25 kΩ cm^{-2}, 2.09 kΩ cm^{-2}, 822.9 Ω cm^{-2}, 348.1 Ω cm^{-2}, and 698.5 Ω cm^{-2} for TiO_2 NRs, $MoSe_2/TiO_2$ NRs-15 s, $MoSe_2/TiO_2$ NRs-30 s, $MoSe_2/TiO_2$ NRs-60 s, $MoSe_2/TiO_2$ NRs-90 s, and $MoSe_2/TiO_2$ NRs-120 s, respectively. This confirms the enhanced charge transfer kinetics over the sample sputtered with $MoSe_2$ for 90 s compared to its counterparts. In contrast, $MoSe_2$ revealed very high charge transfer resistance i.e. 126.3 kΩ cm^{-2}, which is consistent to its inferior photorespone, where currents measured in dark and under illumination were almost identical (Fig. S14a and b).

The flat band potential and type of semiconductor were identified by Mott-Schottky plots. Fig. 8d depicted the Mott-Schottky plots of TiO_2 and the heterostructured electrodes. The flat band potential (E_{fb}) can be defined by the following equation:

$$\frac{1}{C^2} = \frac{2}{qA^2\varepsilon N_D}\left(E - E_{fb} - \frac{K_bT}{q}\right)$$

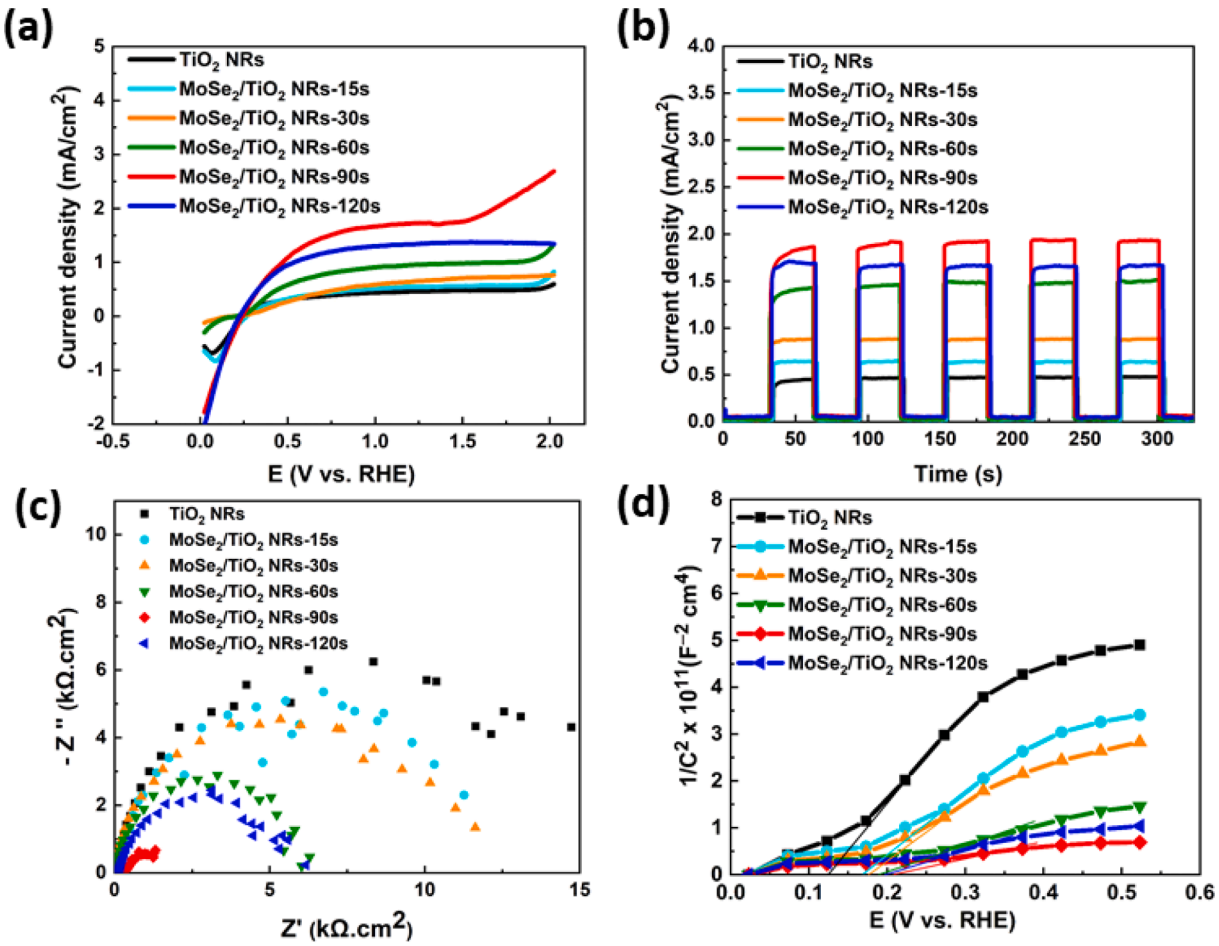

Fig. 8. The electrochemical measurements of TiO_2 NRs and $MoSe_2/TiO_2$ NRs recorded in 1.0 M KOH solution under illumination with simulated sunlight. (a) LSV curves, (b) Transient photocurrent responses at 0.5 V vs. Ag/AgCl, (c) Nyquist impedance plots at 0.5 V vs. Ag/AgCl, and (d) Mott-Schottky plots.

Where C is the space charge capacitance, q is the charge of the electron, N_D is the donor density, E is the applied potential, K_b is the Boltzmann's constant, ε is the dielectric constant of the semiconductor. The linear parts of the plots have positive slopes, implying that the photocatalyst is an n-type semiconductor. The flat band potentials of the heterostructures exhibited a negative shift in their values compared to pure TiO_2 NRs, confirming the enhanced generation of photo-induced charge carriers over the heterostructure compared to pure TiO_2 [35]. The calculated flat band potentials were estimated by extrapolating the linear parts of Mott-Schottky plots ($1/C^2$ vs. E) to the x-axis. The calculated values were 0.12, 0.17, 0.18, 0.19, 0.20, and 0.21 V vs. RHE for TiO_2 NRs, $MoSe_2/TiO_2$ NRs-15 s, $MoSe_2/TiO_2$ NRs-30 s, $MoSe_2/TiO_2$ NRs-60 s, $MoSe_2/TiO_2$ NRs-90 s, $MoSe_2/TiO_2$ NRs-120 s, respectively. The donor concentration can be calculated using the formula:

$$N_d = \left(\frac{2}{e\varepsilon\varepsilon^{\circ}}\right)\left[d\left(\frac{1}{C^2}\right)/dV\right]^{-1}$$

Where N_d, e, ε, and ε° are the donor concentration, charge of the electron (1.6×10^{-19}C), relative dielectric constant of the semiconductor, and the dielectric constant of vacuum (8.85×10^{-14}F cm^{-1}), respectively. The calculated donor concentrations are $1.13x10^{18}$, $1.58x10^{18}$, $1.93x10^{18}$, $5.04x10^{18}$, and $9.24x10^{18}$, and $5.28x10^{18}$ cm^{-3} for TiO_2 NRs, $MoSe_2/TiO_2$ NRs-15 s, $MoSe_2/TiO_2$ NRs-30 s, $MoSe_2/TiO_2$ NRs-60 s, $MoSe_2/TiO_2$ NRs-90 s, $MoSe_2/TiO_2$ NRs-120 s, respectively. The higher value of carriers' concentration on the heterostructure compared to pure TiO_2 NRs can be assigned to boosted charge separation and higher photoresponse.

Based on Mott-Schottky plots, the flat band potentials of TiO_2 NRs and $MoSe_2$ were 0.12 and − 0.52 V vs. RHE, respectively. For n-type semiconductor, it was found that the conduction band potential is almost 0.1 eV lower than E_{fb} [69]. Hence, the E_{CB} of TiO_2 NRs and $MoSe_2$ are + 0.02 V and − 0.42 V vs. RHE, respectively. Hence the valence band potential, E_{VB} can be calculated using the relation: $E_{VB} = E_{fb} + E_g$. The valence band potentials of TiO_2 NRs and $MoSe_2$ will be 3.07 V and 1.47 V vs. RHE, respectively. Based on the band alignment of TiO_2 and $MoSe_2$, they can easily form a Z-scheme heterostructure with enhanced photocatalytic activity.

The photoactivity of pristine TiO_2 NRs and different heterojunctions was investigated by measuring the photocurrent responses at 0 V (Fig. 9a) [70]. It is evident that the coupling of $MoSe_2$ to TiO_2 enhanced the photocatalytic response and $MoSe_2/TiO_2$ NRs-90 s showed the highest value of photocurrent density (38 μA cm^{-2}) compared to the counterparts. This implies its enhanced photocatalytic performance. Contrarily, $MoSe_2$ revealed a negligible photocurrent response, which affirms its inferior photocatalytic activity (Fig. S14c).

Stability is a crucial factor for applying a semiconductor as a photocatalyst. Fig. 9b represents the variation of photocurrent response of $MoSe_2/TiO_2$ NRs-90 s with time. Notably, the photocurrent density revealed no significant decay from its initial value after illumination with simulated sunlight for 2000 s. This implies the enhanced photostability of the heterostructure.

Based on the reported results, the charge transfer process can be represented according to the mechanism shown in Fig. 10. Under light irradiation, both $MoSe_2$ and TiO_2 can be excited. The electrons in the valence band of TiO_2 or $MoSe_2$ can be excited to the conduction band

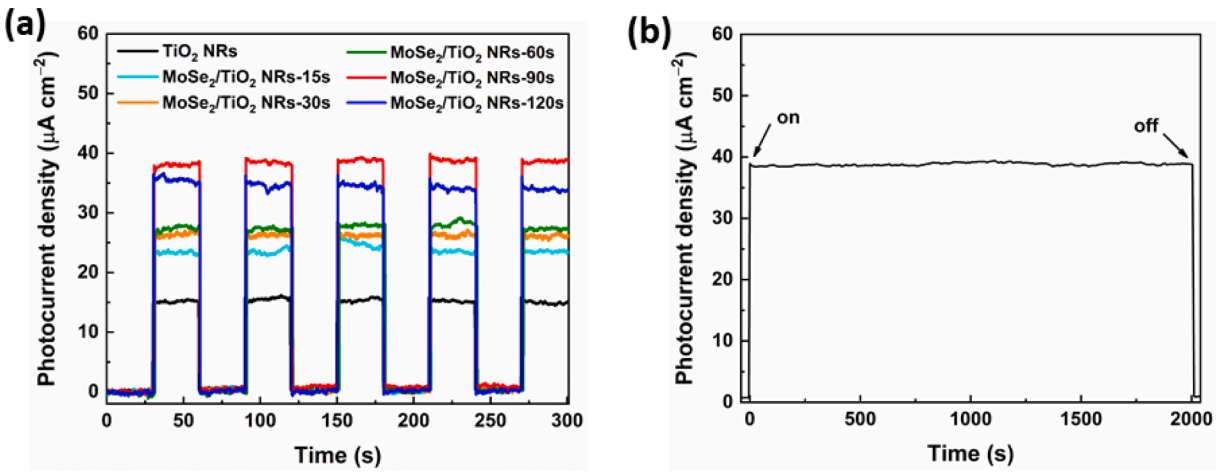

Fig. 9. (a) The photocurrent responses of studied photocatalysts and (b) The photocurrent stability of $MoSe_2/TiO_2$ NRs-90 s.

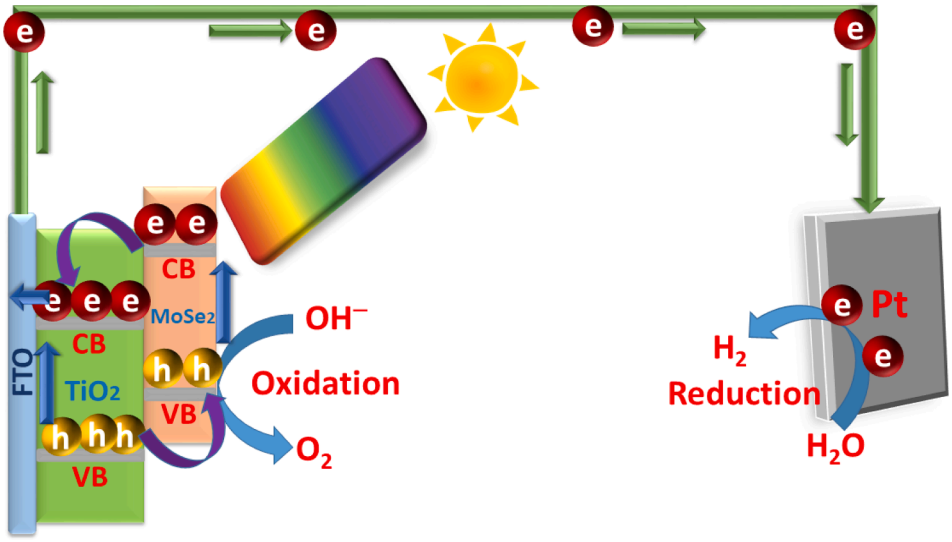

Fig. 10. The schematic diagram for the charge transfer mechanism at the $MoSe_2/TiO_2$ heterojunction.

leaving vacancies (holes) in the valence band. Owing to the suitable band alignment, the photo-generated electrons transfer from the conduction band of $MoSe_2$ to the conduction band of TiO_2, which enhances the charge separation and retard the charge recombination. The external electric field facilitates the transfer of electrons to the cathode, where the reduction process takes place. On the other hand, holes are transferred from the VB of TiO_2 to the valence band of $MoSe_2$, where oxidation occurs. This efficient charge separation secures a low recombination rate of photo-induced charge carriers and efficient charge transfer, enhancing the photocatalytic activity for the heterostructure compared to pure TiO_2.

4. Conclusions

$MoSe_2$/1D TiO_2 NRs heterostructures were synthesized via deposition of $MoSe_2$ nanosheets by RF magnetron sputtering on TiO_2 NRs assembly synthesized by hydrothermal method. $MoSe_2$ was grown as nanosheets, which maximizes the number of defects and active sites. The optical properties and the photocatalytic performance of the heterostructures, were greatly influenced by the thickness of the $MoSe_2$ layer, which was optimized by variation of the sputtering time (the 90 s is the optimum time). The heterojunction afforded outstanding photocatalytic performance compared to pristine TiO_2 NRs. This can be attributed to the decreased band gap and enhanced charge separation, which suppress the recombination of the photo-generated charge carriers and increase their lifetime. Furthermore, the synergy between the 1D nanoarchitecture of TiO_2 and the tailored loading of $MoSe_2$ nanosheets on the surface of TiO_2 NRs enhances the electron transfer and boosts the catalytic activity towards OER.

CRediT authorship contribution statement

Yahia H. Ahmad: Data curation, Formal analysis, Writing – original draft. **Fadi Z. Kamand:** Data curation, Formal analysis, Writing – original draft. **Atef Zekri:** Methodology, Data curation. **Kyu-Jung Chae:** Writing – review & editing, Funding acquisition, Project administration. **Brahim Aïssa:** Methodology, Data curation, Validation, Resources. **Siham Y. Al-Qaradawi:** Funding acquisition, Project administration, Writing – review & editing, Supervision.

Declaration of Competing Interest

The authors declare that they have no known competing financial interests or personal relationships that could have appeared to influence the work reported in this paper.

Data availability

Data will be made available on request.

Acknowledgment

This work was made possible by NPRP Grant no. NPRP 12S-0304-190218 from the Qatar National Research Fund (a member of the Qatar Foundation). The statements made herein are solely the responsibility of the authors.

Open Access funding provided by the Qatar National Library.

Appendix A. Supplementary material

Supplementary data to this article can be found online at https://doi.org/10.1016/j.apsusc.2023.157205.

References

[1] F. Dawood, M. Anda, G.M. Shafiullah, Hydrogen production for energy: An overview, Int. J. Hydrog. Energy 45 (2020) 3847–3869.
[2] C. Acar, I. Dincer, Review and evaluation of hydrogen production options for better environment, J. Clean. Prod. 218 (2019) 835–849.
[3] S. Wang, A. Lu, C.-J. Zhong, Hydrogen production from water electrolysis: role of catalysts, Nano Converg. 8 (2021) 4.
[4] Y. Zang, S. Huang, B. Yang, G. Chen, X. Liu, N. Zhang, Constructing collaborative interface between Mo_2N and NiS as efficient bifunctional electrocatalysts for overall water splitting, Appl. Surf. Sci. 611 (2023), 155656.
[5] W. Yang, R.R. Prabhakar, J. Tan, S.D. Tilley, J. Moon, Strategies for enhancing the photocurrent, photovoltage, and stability of photoelectrodes for photoelectrochemical water splitting, Chem. Soc. Rev. 48 (2019) 4979–5015.
[6] A. Fujishima, K. Honda, Electrochemical Photolysis of Water at a Semiconductor Electrode, Nature 238 (1972) 37–38.
[7] Y. Ma, X. Wang, Y. Jia, X. Chen, H. Han, C. Li, Titanium Dioxide-Based Nanomaterials for Photocatalytic Fuel Generations, Chem. Rev. 114 (2014) 9987–10043.
[8] A.T. Montoya, E.G. Gillan, Enhanced Photocatalytic Hydrogen Evolution from Transition-Metal Surface-Modified TiO2, ACS Omega 3 (2018) 2947–2955.
[9] Y.H. Ahmad, A.T. Mohamed, M.H. Sliem, A.M. Abdullah, S.Y. Al-Qaradawi, Enhanced photocatalytic performance of WON@porous TiO_2 nanofibers towards sunlight-assisted degradation of organic contaminants, RSC Adv. 8 (2018) 32747–32755.
[10] P.S. Basavarajappa, S.B. Patil, N. Ganganagappa, K.R. Reddy, A.V. Raghu, C. V. Reddy, Recent progress in metal-doped TiO_2, non-metal doped/codoped TiO_2 and TiO_2 nanostructured hybrids for enhanced photocatalysis, Int. J. Hydrog. Energy 45 (2020) 7764–7778.
[11] M. Ge, J. Cai, J. Iocozzia, C. Cao, J. Huang, X. Zhang, J. Shen, S. Wang, S. Zhang, K.-Q. Zhang, Y. Lai, Z. Lin, A review of TiO_2 nanostructured catalysts for sustainable H_2 generation, Int. J. Hydrog. Energy 42 (2017) 8418–8449.
[12] A. Meng, L. Zhang, B. Cheng, J. Yu, Dual Cocatalysts in TiO_2 Photocatalysis, Adv. Mater. 31 (2019) 1807660.
[13] C. Xia, T. Hong Chuong Nguyen, X. Cuong Nguyen, S. Young Kim, D.L.T. Nguyen, P. Raizada, P. Singh, V.-H. Nguyen, C. Chien Nguyen, V. Chinh Hoang, Q. Van Le, Emerging cocatalysts in TiO_2-based photocatalysts for light-driven catalytic hydrogen evolution: Progress and perspectives, Fuel 307 (2022), 121745.
[14] K. Parul, R. Kaur, P.P. Badru, S. Singh, Kaushal, Photodegradation of organic pollutants using heterojunctions: A review, J. Environ. Chem. Eng. 8 (2020), 103666.
[15] X. Chai, H. Zhang, Q. Pan, J. Bian, Z. Chen, C. Cheng, 3D ordered urchin-like TiO_2@Fe_2O_3 arrays photoanode for efficient photoelectrochemical water splitting, Appl. Surf. Sci. 470 (2019) 668–676.
[16] T. Heine, Transition Metal Chalcogenides: Ultrathin Inorganic Materials with Tunable Electronic Properties, Acc. Chem. Res. 48 (2015) 65–72.
[17] L. Cao, S. Yang, W. Gao, Z. Liu, Y. Gong, L. Ma, G. Shi, S. Lei, Y. Zhang, S. Zhang, R. Vajtai, P.M. Ajayan, Direct Laser-Patterned Micro-Supercapacitors from Paintable MoS_2 Films, Small 9 (2013) 2905–2910.
[18] G. Eda, S.A. Maier, Two-Dimensional Crystals: Managing Light for Optoelectronics, ACS Nano 7 (2013) 5660–5665.
[19] Z.-B. Zhai, K.-J. Huang, X. Wu, Superior mixed Co-Cd selenide nanorods for high performance alkaline battery-supercapacitor hybrid energy storage, Nano Energy 47 (2018) 89–95.
[20] Y. Guo, T. Park, J.W. Yi, J. Henzie, J. Kim, Z. Wang, B. Jiang, Y. Bando, Y. Sugahara, J. Tang, Y. Yamauchi, Nanoarchitectonics for Transition-Metal-Sulfide-Based Electrocatalysts for Water Splitting, Adv. Mater. 31 (2019) 1807134.
[21] E.T. Sayed, M.A. Abdelkareem, A. Bahaa, T. Eisa, H. Alawadhi, S. Al-Asheh, K.-J. Chae, A.G. Olabi, Synthesis and performance evaluation of various metal chalcogenides as active anodes for direct urea fuel cells, Renew. Sustain. Energy Rev. 150 (2021), 111470.
[22] A. Bahaa, M.A. Abdelkareem, H. Al naqbi, A. Yousef Mohamed, P.A. Shinde, B.A. A. Yousef, E.T. Sayed, H. Alawadhi, K.-J. Chae, S. Al-Asheh, A.G. Olabi, High energy storage quasi-solid-state supercapacitor enabled by metal chalcogenide nanowires and iron-based nitrogen-doped graphene nanostructures, J. Colloid Interface Sci. 608 (2022) 711–719.
[23] S. Manzeli, D. Ovchinnikov, D. Pasquier, O.V. Yazyev, A. Kis, 2D transition metal dichalcogenides, Nat. Rev. Mater. 2 (2017) 17033.
[24] R. Li, Y. Cheng, W. Huang, Recent Progress of Janus 2D Transition Metal Chalcogenides: From Theory to Experiments, Small 14 (2018) 1802091.
[25] T. Eisa, M.A. Abdelkareem, D.A. Jadhav, H.O. Mohamed, E.T. Sayed, A.G. Olabi, P. Castaño, K.-J. Chae, Critical review on the synthesis, characterization, and application of highly efficient metal chalcogenide catalysts for fuel cells, Prog. Energy Combust. Sci. 94 (2023), 101044.
[26] S. Tongay, J. Zhou, C. Ataca, K. Lo, T.S. Matthews, J. Li, J.C. Grossman, J. Wu, Thermally Driven Crossover from Indirect toward Direct Bandgap in 2D Semiconductors: $MoSe_2$ versus MoS_2, Nano Lett. 12 (2012) 5576–5580.
[27] Y. Cheng, J. Zhang, C. Chen, X. Xiong, J. Zeng, J. Xi, Y.-J. Yuan, Z. Ji, A novel 2D/2D $MoSe_2$/SnSe heterojunction photocatalyst with large carrier transmission channel shows excellent photoelectrochemical performance, Appl. Surf. Sci. 563 (2021), 150311.
[28] Y. Yu, G.-H. Nam, Q. He, X.-J. Wu, K. Zhang, Z. Yang, J. Chen, Q. Ma, M. Zhao, Z. Liu, F.-R. Ran, X. Wang, H. Li, X. Huang, B. Li, Q. Xiong, Q. Zhang, Z. Liu, L. Gu, Y. Du, W. Huang, H. Zhang, High phase-purity 1T′-MoS_2- and 1T′-$MoSe_2$-layered crystals, Nat. Chem. 10 (2018) 638–643.
[29] J. Kang, S. Tongay, J. Zhou, J. Li, J. Wu, Band offsets and heterostructures of two-dimensional semiconductors, Appl. Phys. Lett. 102 (2013), 012111.
[30] C. Tsai, K. Chan, F. Abild-Pedersen, J.K. Nørskov, Active edge sites in $MoSe_2$ and WSe_2 catalysts for the hydrogen evolution reaction: a density functional study, Phys. Chem. Chem. Phys. 16 (2014) 13156–13164.
[31] Y. Wu, M. Xu, X. Chen, S. Yang, H. Wu, J. Pan, X. Xiong, CTAB-assisted synthesis of novel ultrathin $MoSe_2$ nanosheets perpendicular to graphene for the adsorption and photodegradation of organic dyes under visible light, Nanoscale 8 (2016) 440–450.
[32] L. Wu, S. Shi, Q. Li, X. Zhang, X. Cui, TiO_2 nanoparticles modified with 2D $MoSe_2$ for enhanced photocatalytic activity on hydrogen evolution, Int. J. Hydrog. Energy 44 (2019) 720–728.
[33] X. Zheng, L. Yang, Y. Li, L. Yang, S. Luo, Direct Z-scheme $MoSe_2$ decorating TiO_2 nanotube arrays photocatalyst for water decontamination, Electrochim. Acta 298 (2019) 663–669.
[34] R. Zazpe, R. Krumpolec, H. Sopha, J. Rodriguez-Pereira, J. Charvot, L. Hromádko, E. Kolíbalová, J. Michalička, D. Pavliňák, M. Motola, J. Přikryl, M. Krbal, F. Bureš, J.M. Macak, Atomic Layer Deposition of $MoSe_2$ Nanosheets on TiO_2 Nanotube Arrays for Photocatalytic Dye Degradation and Electrocatalytic Hydrogen Evolution, ACS Appl. Nano Mater. 3 (2020) 12034–12045.
[35] T. Li, P. Zhang, H. He, Z. Wang, X. Tu, D.D. Dionysiou, Highly efficient photoelectrocatalytic degradation of cefotaxime sodium on the $MoSe_2$/TiO_2 nanotubes photoanode with abundant oxygen vacancies, J. Solid State Chem. 303 (2021), 122455.
[36] X. Wang, Y. Gong, G. Shi, W.L. Chow, K. Keyshar, G. Ye, R. Vajtai, J. Lou, Z. Liu, E. Ringe, B.K. Tay, P.M. Ajayan, Chemical Vapor Deposition Growth of Crystalline Monolayer $MoSe_2$, ACS Nano 8 (2014) 5125–5131.
[37] Y. Cheng, Y. Zhao, H. Zhao, H. Lv, X. Qi, J. Cao, G. Ji, Y. Du, Engineering morphology configurations of hierarchical flower-like $MoSe_2$ spheres enable excellent low-frequency and selective microwave response properties, Chem. Eng. J. 372 (2019) 390–398.
[38] A. Jäger-Waldau, M. Lux-Steiner, R. Jäger-Waldau, R. Burkhardt, E. Bucher, Composition and morphology of $MoSe_2$ thin films, Thin Solid Films 189 (1990) 339–345.
[39] M. Kristl, M. Drofenik, Synthesis of nanocrystalline $MoSe_2$ by sonochemical reaction of Se with $Mo(CO)_6$, Inorg. Chem. Commun. 6 (2003) 68–70.
[40] X. Cao, H. Li, G. Li, X. Gao, Electrocatalytically active $MoSe_2$ counter electrode prepared in situ by magnetron sputtering for a dye-sensitized solar cell, Chin. J. Catal. 40 (2019) 1360–1365.
[41] P. Han, B. Sun, S. Cheng, F. Yu, B. Jiao, Q. Wu, Preparation of $MoSe_2$ nano-islands array embedded in a TiO_2 matrix for photo-regulated resistive switching memory, J. Alloys Compd. 664 (2016) 619–625.
[42] X. Xiong, J. Zhang, C. Chen, S. Yang, J. Lin, J. Xi, Z. Kong, Novel n-MoSSe/p-Co_3O_4 Z-scheme heterojunction photocatalyst for highly boosting photoelectrochemical and photocatalytic activity, J. Alloys Compd. 926 (2022), 166863.
[43] Y.H. Ahmad, A.S. Abu Hatab, A.T. Mohamed, M.S. Al-Kuwari, A.S. Aljaber, S.Y. Al-Qaradawi, Microwave-Assisted Solvothermal Synthesis of Mo-Doped TiO_2 with Exceptional Textural Properties and Superior Adsorption Kinetics, Nanomaterials (2022) 2051.
[44] M. Ge, C. Cao, J. Huang, S. Li, Z. Chen, K.-Q. Zhang, S.S. Al-Deyab, Y. Lai, A review of one-dimensional TiO_2 nanostructured materials for environmental and energy applications, J. Mater. Chem. A 4 (2016) 6772–6801.
[45] A. Prathan, J. Sanglao, T. Wang, C. Bhoomanee, P. Ruankham, A. Gardchareon, D. Wongratanaphisan, Controlled Structure and Growth Mechanism behind Hydrothermal Growth of TiO_2 Nanorods, Sci. Rep. 10 (2020) 8065.
[46] H. Kim, B.L. Yang, Effect of seed layers on TiO_2 nanorod growth on FTO for solar hydrogen generation, Int. J. Hydrog. Energy 40 (2015) 5807–5814.
[47] Y. Wang, L. Zhang, K. Deng, X. Chen, Z. Zou, Low Temperature Synthesis and Photocatalytic Activity of Rutile TiO_2 Nanorod Superstructures, J. Phys. Chem. C 111 (2007) 2709–2714.
[48] H. Zhang, L. Ma, J. Ming, B. Liu, Y. Zhao, Y. Hou, Z. Ding, C. Xu, Z. Zhang, J. Long, Amorphous $Ta_2O_xN_y$-enwrapped TiO_2 rutile nanorods for enhanced solar photoelectrochemical water splitting, Appl. Catal. B Environ. 243 (2019) 481–489.

[49] G. Zhao, P. Li, K. Rui, Y. Chen, S.X. Dou, W. Sun, $CoSe_2/MoSe_2$ Heterostructures with Enriched Water Adsorption/Dissociation Sites towards Enhanced Alkaline Hydrogen Evolution Reaction, Chem. Eur. J. 24 (2018) 11158–11165.
[50] B. Bharti, S. Kumar, H.-N. Lee, R. Kumar, Formation of oxygen vacancies and Ti^{3+} state in TiO_2 thin film and enhanced optical properties by air plasma treatment, Sci. Rep. 6 (2016) 32355.
[51] S. Jain, J. Shah, N.S. Negi, C. Sharma, R.K. Kotnala, Significance of interface barrier at electrode of hematite hydroelectric cell for generating ecopower by water splitting, Int. J. Energy Res. 43 (2019) 4743–4755.
[52] T.K. Das, P. Ilaiyaraja, C. Sudakar, Template assisted nanoporous TiO_2 nanoparticles: The effect of oxygen vacancy defects on photovoltaic performance of DSSC and QDSSC, Sol. Energy 159 (2018) 920–929.
[53] X. Zhang, Y. Zeng, W. Shi, Z. Tao, J. Liao, C. Ai, H. Si, Z. Wang, A.C. Fisher, S. Lin, S-scheme heterojunction of core–shell biphase (1T–2H)-$MoSe_2/TiO_2$ nanorod arrays for enhanced photoelectrocatalytic production of hydrogen peroxide, Chem. Eng. J. 429 (2022), 131312.
[54] W.-K. Jo, T. Sivakumar Natarajan, Facile Synthesis of Novel Redox-Mediator-free Direct Z-Scheme $CaIn_2S_4$ Marigold-Flower-like/TiO_2 Photocatalysts with Superior Photocatalytic Efficiency, ACS Appl. Mater. Interfaces 7 (2015) 17138–17154.
[55] H.Z. Asl, S.M. Rozati, High-quality spray-deposited fluorine-doped tin oxide: effect of film thickness on structural, morphological, electrical, and optical properties, Appl. Phys. A 125 (2019) 689.
[56] H. Arami, M. Mazloumi, R. Khalifehzadeh, S.K. Sadrnezhaad, Sonochemical preparation of TiO_2 nanoparticles, Mater. Lett. 61 (2007) 4559–4561.
[57] I. Takahashi, Electronic resonance and photoemission study of nitrogen doped TiO_2 rutile (110) single crystals, Appl. Surf. Sci. 259 (2012) 320–323.
[58] S. Sathiyan, H. Ahmad, W.Y. Chong, S.H. Lee, S. Sivabalan, Evolution of the Polarizing Effect of $MoSe_2$, IEEE Photonics J. 7 (2015) 1–10.
[59] U. Balachandran, N.G. Eror, Raman spectra of titanium dioxide, J. Solid State Chem. 42 (1982) 276–282.
[60] J.C. Parker, R.W. Siegel, Calibration of the Raman spectrum to the oxygen stoichiometry of nanophase TiO_2, Appl. Phys. Lett. 57 (1990) 943–945.
[61] S. Wang, J. Xu, H. Ding, S. Pan, Y. Zhang, G. Li, Facile synthesis of nitrogen self-doped rutile TiO_2 nanorods, CrystEngComm 14 (2012) 7672–7679.
[62] S. Dey, A. Chakravorty, S.B. Mishra, N. Khatun, A. Hazra, B.R.K. Nanda, C. Sudakar, D. Kabiraj, S.C. Roy, Localized thermal spike driven morphology and electronic structure transformation in swift heavy ion irradiated TiO_2 nanorods, Nanoscale Adv. 4 (2022) 241–249.
[63] K. Lv, H. Zuo, J. Sun, K. Deng, S. Liu, X. Li, D. Wang, (Bi, C and N) codoped TiO_2 nanoparticles, J. Hazard. Mater. 161 (2009) 396–401.
[64] A. Wolcott, W.A. Smith, T.R. Kuykendall, Y. Zhao, J.Z. Zhang, Photoelectrochemical Water Splitting Using Dense and Aligned TiO_2 Nanorod Arrays, Small 5 (2009) 104–111.
[65] H. Li, C. Yang, X. Wang, J. Zhang, J. Xi, G. Du, Z. Ji, Mixed 3D/2D dimensional TiO_2 nanoflowers/$MoSe_2$ nanosheets for enhanced photoelectrochemical hydrogen generation, J. Am. Ceram. Soc. 103 (2020) 1187–1196.
[66] D. Cao, Y. Wang, M. Qiao, X. Zhao, Enhanced photoelectrocatalytic degradation of norfloxacin by an $Ag_3PO_4/BiVO_4$ electrode with low bias, J. Catal. 360 (2018) 240–249.
[67] Y.H. Ahmad, K. Eid, K.A. Mahmoud, S.Y. Al-Qaradawi, Controlled design of PtPd nanodendrite ornamented niobium oxynitride nanosheets for solar-driven water splitting, New J. Chem. 42 (2018) 14239–14245.
[68] A.S. Abu Hatab, Y.H. Ahmad, M. Ibrahim, A. Elsafi Ahmed, M.B. Abdul Rahman, S. Y. Al-Qaradawi, MOF-Derived Cobalt@Mesoporous Carbon as Electrocatalysts for Oxygen Evolution Reaction: Impact of Organic Linker, Langmuir 39 (2023) 1123–1134.
[69] X. Xiong, J. Zhang, C. Chen, S. Yang, J. Lin, J. Xi, Z. Kong, Novel 0D/2D Bi_2WO_6/MoSSe Z-scheme heterojunction for enhanced photocatalytic degradation and photoelectrochemical activity, Ceram. Int. 48 (2022) 31970–31983.
[70] C. Chen, J. Zhang, X. Xiong, J. Lin, S. Yang, J. Xi, Z. Kong, A novel Z-type multidimensional $FeSe_2$/CuSe heterojunction photocatalyst with high photocatalytic and photoelectrochemical performance, Int. J. Hydrog. Energy 47 (2022) 28879–28893.